Earth and Planetary Science Letters 527 (2019) 115783

Contents lists available at ScienceDirect

Earth and Planetary Science Letters

www.elsevier.com/locate/epsl

Permeability evolution during non-isothermal compaction in volcanic conduits and tuffisite veins: Implications for pressure monitoring of volcanic edifices

S. Kolzenburg [a,b,c,*], A.G. Ryan [d], J.K. Russell [d]

[a] Ludwig-Maximilians-University Munich, Department of Earth and Environmental Sciences, Section for Mineralogy, Petrology and Geochemistry, Theresienstraße 41, 80333 München, Germany
[b] McGill University, Department of Earth and Planetary Sciences, 3450 University Street, H3A 0E8 Montreal, Quebec, Canada
[c] University at Buffalo, Department of Geology, 126 Cooke Hall, Buffalo, NY 14260, United States of America
[d] Volcanology and Petrology Laboratory, Earth, Ocean and Atmospheric Sciences, University of British Columbia, 2020-2207 Main Mall, Vancouver, V6T 1Z4, Canada

ARTICLE INFO

Article history:
Received 26 January 2019
Received in revised form 15 August 2019
Accepted 16 August 2019
Available online 11 September 2019
Editor: T.A. Mather

Keywords:
volcano monitoring
thermal modeling
welding
compaction
viscous sintering
permeability

ABSTRACT

Explosive volcanic eruptions are destructive geological phenomena that pose hazards of significant socioeconomic impact and potential loss of life. Effective risk mitigation and decision making prior to and during volcanic crises require real-time monitoring of gas overpressure – the single most important driving force for explosive eruptions. Development and release of gas overpressure are regulated by gas loss through permeable pathways that are inherently transient.

Here, we use geometry-dependent conductive cooling models, in concert with the most up-to-date welding and permeability models, to assess the potential for "freezing in" permeability within (1) conduit-filling pyroclastic deposits and (2) tuffisite veins within the edifice. We find that both geometry and dimension of each deposit dictate its thermal evolution and, with that, its transient outgassing capacity. Rapid cooling of thin sheet-like tuffisite veins preserves high porosities and permeabilities. In contrast, wide cylindrical conduit-filling deposits cool slowly and permeability is annihilated over a period of minutes to hours. This highlights that conduit-filling deposits lose their outgassing capacity through welding, while tuffisite veins (previously thought to rapidly seal) can form long-lived outgassing features. We use the model results to calculate the time dependent gas flow partitioning between both degassing lithologies. Based on the reconstructed outgassing pattern we outline the potential to use the gas flow balance between the central conduit and distal fumaroles fed by tuffisite veins as a simple tool to monitor gas overpressure within a volcanic edifice.

1. Introduction

Explosive volcanic eruptions are destructive geological phenomena that pose hazards of significant socioeconomic impact (pyroclastic flows, tephra dispersal) and potential loss of life. Risk is especially high in densely populated areas where monitoring infrastructure is scarce. Effective risk mitigation and decision making prior to and during volcanic crises require real-time monitoring of gas overpressure – the single most important driving force for explosive eruptions.

All silicate melts exsolve volatiles during ascent and eruption. Volcanic overpressure develops when the volume of gas released from the magma exceeds the outgassing capacity of the volcanic system which, itself, depends on sustained permeable pathways (Farquharson et al., 2017b; Jaupart and Allègre, 1991). When this (over)-pressure exceeds the strength of the confining rock mass, portions of the edifice fail, resulting in rapid decompression of the magma and explosive eruption (Alidibirov and Dingwell, 1996; Rutherford et al., 1985)

Permeable pathways (i.e. networks of interconnected void space, including bubbles, cracks and spaces between crystals and clasts) permit exsolved gases to vent from the magma through the volcanic edifice. The abundance and outgassing capacity of permeable materials therefore moderates gas pressurization and reduces the potential for explosive eruption (Castro et al., 2012;

* Corresponding author at: Ludwig-Maximilians-University Munich, Department of Earth and Environmental Sciences, Section for Mineralogy, Petrology and Geochemistry, Theresienstraße 41, 80333 München, Germany.
E-mail address: skolzenburg@gmail.com (S. Kolzenburg).

https://doi.org/10.1016/j.epsl.2019.115783

Farquharson et al., 2017b; Jaupart and Allègre, 1991; Kennedy et al., 2010; Kolzenburg and Russell, 2014). Permeable pathways can include connected bubble networks in the ascending magma (Klug and Cashman, 1996; Rust and Cashman, 2004), networks of cracks and void spaces in the pyroclastic material that fill the volcanic conduit (Chevalier et al., 2017; Eichelberger et al., 1986; Kennedy et al., 2010; Kolzenburg and Russell, 2014), and tuffisite veins, representing volcanic hydro-fractures propped open by fragmental juvenile and accessory material (Heiken et al., 1988; Kendrick et al., 2016; Kolzenburg et al., 2012; Saubin et al., 2016; Stasiuk et al., 1996; Tuffen et al., 2003).

Most intermediate to silicic volcanoes that produce Vulcanian to Plinian eruptions maintain post-eruptive permeability. Evidence for efficient, long lived permeable networks includes: 1) pervasive, long lived and large volume fumarole outgassing from explosive volcanoes (Edmonds et al., 2003; Holland et al., 2011; Taran et al., 2002), 2) chemical variations within clasts in tuffisite veins that document active outgassing on the timescale of hours to days (Berlo et al., 2013; Castro et al., 2012; Paisley et al., 2019), 3) changes in fumarole composition and volcanic geothermal spring water chemistry reflecting changes in magma outgassing patterns (Taran et al., 2002), and 4) constant or periodic outgassing through well established and long lived lava domes without an associated larger explosive event (Holland et al., 2011; Lavallée et al., 2012).

In contrast, experiments and models (Farquharson et al., 2017b; Grunder and Russell, 2005; Kolzenburg and Russell, 2014; Russell and Quane, 2005; Wadsworth et al., 2014) suggest the porosity and permeability of volcanic materials to be ephemeral when held above their glass transition temperatures (T_g). This loss of permeability at high temperatures has also been observed in some silicic vents (Schipper et al., 2013). At temperatures in excess of T_g, densification processes, involving reduction of pore space and permeability loss, can operate on timescales of minutes to hours via viscous annealing and compaction (i.e. sintering or welding (Grunder and Russell, 2005; Wadsworth et al., 2014)). Rapid densification and loss of permeability has the inevitable consequence of leading to rising gas overpressures and renewed explosivity (Edmonds et al., 2003; Farquharson et al., 2017b; Jaupart and Allègre, 1991; Kolzenburg and Russell, 2014; Massol and Jaupart, 1999).

One way to reconcile observations of natural systems (sustained volcanic outgassing) and experimental results (rapid loss of permeability) is to consider the thermal histories of the pyroclastic deposits that make up the volcanic edifice. Here, we explore how geometry and size affect the extent and timescale of welding during cooling of hot pyroclastic deposits, including: i) conduit filling deposits and ii) networks of tuffisite veins within the host volcanic edifice (i.e. emplaced within cool country rock rather than within the magma column). Specifically, we have coupled a model for viscous compaction to conductive cooling models for these two geometries. Our results elucidate the timescales for heat loss *vs.* viscous compaction and explore the implications for annihilating or preserving permeability and, therewith, controlling eruption style.

2. Methods: a series of models

2.1. Model overview

Our analysis of welding and compaction processes couples four separate types of models, Fig. 1; model parameters are shown in Table 1. We include: i) thermal models for cooling of conduits and tuffisite sheets at their respective relevant dimension, Tables A1 and A2 (e.g., Carslaw and Jaeger, 1959; Crank, 1979, ii) chemical models for the melt properties (e.g., H_2O solubility, viscosity, T_g;

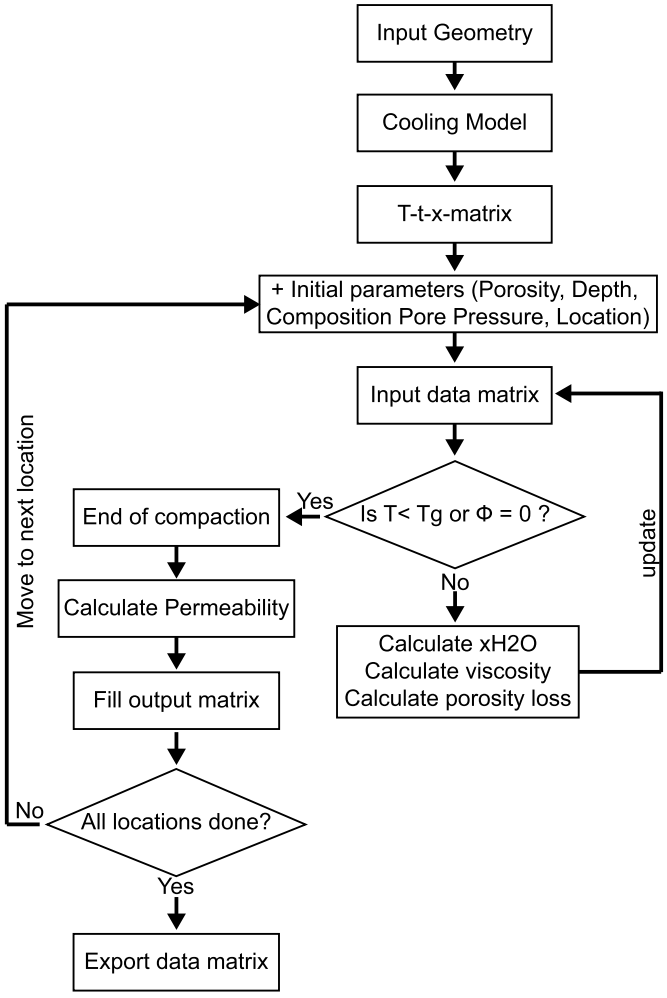

Fig. 1. Flow chart showing the architecture of the numerical model.

(Giordano et al., 2008; Liu et al., 2005), iii) models for porosity-permeability relationships (Wright and Cashman, 2014), and iv) a viscous compaction model (Russell and Quane, 2005). Combined, these coupled models provide a systematic description of the parameters guiding the change in permeability of conduit infill and tuffisite veins during welding and compaction. We have organized these models in series so they predict welding progress as a function of time in iterative intervals of 1 Hz.

Fig. 1 shows a schematic representation of the model organization: for each time step the model updates the temperature and porosity, and calculates the temperature-dependent solubility of water in the melt (Liu et al., 2005). Solubility results are forwarded to the melt viscosity model of Giordano et al. (2008) to recover the temperature- and H_2O-dependent melt viscosity and T_g. If the time step in model temperature remains above T_g, the viscosity value is fed into the welding and compaction model of Russell and Quane (2005) and the change in porosity over this time interval is calculated and used in the next iteration (i.e. Δt) of the model. If the model time step temperature is below T_g the current porosity value is accepted as the final porosity and marks the cessation of welding and compaction (i.e. the "frozen in" porosity). The deposit permeability is then calculated after Wright and Cashman (2014) to retrieve the "frozen in" permeability. These iterations are repeated until either $T < T_g$ or $\Phi = 0$. While magmas commonly retain small amounts of residual porosity when reaching the impermeable state, we use 0 as a numerical stopping criterion for the compaction model and do not define an arbitrary final porosity as a stopping criterion. Variations in this parameter have no effect on

the implications outlined in the discussion since the permeabilities expected at these low porosities are well below those relevant for the discussion ($<10^{-16}$ m^2). Note that this model assumes that if material is emplaced at $T < T_g$ porosity and permeability are preserved since compaction and porosity reduction are modeled as a viscous process. This model does not consider the effect of mineral precipitation or solid state diffusion since they act on much longer timescales; for examples see Taran et al. (2002) and Ryan et al. (2018), respectively. Further, this model describes one emplacement event and does not consider repeated fragmentation and healing of either deposit.

2.2. Thermal modeling

2.2.1. Constraints on model geometry and dimension

Rates of heat dissipation are dependent on the geometry (i.e. surface to volume ratio) and dimensions of the cooling body. Here, we have compiled the available literature to constrain the dimensions of volcanic conduits (Table A1) and tuffisite veins (Table A2) associated with explosive volcanism. Constraints of conduit diameters during active explosive eruptions are inherently difficult as they either rely on post eruptive measurements or inferences from the eruption column height and width (see reference list in Table A1). The largest conduits reach 100–200 m in diameter (Sigurdsson et al., 2015), however, the majority are reported at less than 40–60 m in diameter (Holland et al., 2011; Lavallée et al., 2012; Rutherford et al., 1985; Sigurdsson et al., 2015). Conduit diameters supporting Vulcanian to Plinian eruptions, which are most relevant to the welding, compaction and pressurization processes, are generally narrower, and lie between 10–20 m (Sigurdsson et al., 2015). We have adopted 10 m as the conduit diameter for our cooling and welding/compaction modeling to maximize the potential for preserving permeability in the conduit during cooling.

Estimates of characteristic tuffisite vein thickness are primarily based on measurements of vein material preserved in blocks ejected from andesitic to rhyolitic volcanoes during Vulcanian to Plinian eruptions (Table A2). Reported thicknesses vary between 0.001 m and 0.2 m (Berlo et al., 2013; Castro et al., 2012; Farquharson et al., 2015; Kendrick et al., 2016; Kolzenburg et al., 2012; Saubin et al., 2016). Where tuffisite veins are observed within dissected extinct volcanic conduits and their margins (e.g., Torfajökull, Tuffen et al., 2003 and Mule Creek, Stasiuk et al., 1996), measurements broadly agree with the range of values reported for tuffisite preserved in ejected blocks. Only in rare cases do vein thicknesses exceed 0.2 m: in a drill hole into the Inyo Domes (Heiken et al., 1988) vein thicknesses up to 0.4 m are reported, and in the wall rocks of the Schwäbische Alp volcanoes, Germany (Cloos, 1941) vein thicknesses reach 0.7 m. Based on the available data we assign 0.1 m as an average tuffisite thickness for our cooling and welding/compaction modeling.

2.2.2. Cooling model

We employ two separate, geometry-dependent models to simulate cooling histories: one for cylinders (i.e. conduits), and one for sheets (i.e. tuffisites). We assume cooling of the conduit and tuffisite veins is dominated by conduction and the effects of convective cooling or advective heat loss are not considered. Any contribution of latent heat of crystallization is assumed to be negligible because the welding and compaction processes in silicic melts operate on much faster timescales than crystallization (Vetere et al., 2015). We also assume the thermal diffusivities (κ) of each rock type (i.e. fragmental material and country rock) do not change in space or with time; thus we assign an average value for each rock type (Table 1). We employ a 1D transient model for the thermal evolution of conduit margins (see Heap et al., 2017 and Schauroth et al., 2016 for details and the reasoning thereof).

Table 1
Model parameters.

Symbol	Description	Values in model
Φ_{cr}	Crystal fraction	0
Φ_p	Porosity fraction	0.4
K	Thermal diffusivity (m^2/s)	10^{-6}
a	Conduit radius (m)	5 ±2.5
b	Vein halfwidth (m)	0.05 ±0.025
T_{cr}	Country rock temperature (C)	150
Ti	Emplacement temperature (C)	750–800
P	Bulk density (kg/m^3)	2500
P	Pore pressure (MPa)	1
o	Load stress (MPa)	depth dependent
At	Cooling interval (s)	1

We model the cooling of conduit-filling pyroclastic materials, approximated as a cylinder, using an equation for an infinite cylindrical body (equation 3.11; Crank, 1979):

$$T(t) = (T_i - T_{cr})\left\{1 - \exp\left(\frac{-a^2}{4\kappa t}\right)\right\} + T_{cr} \quad (1)$$

where T is the transient temperature at the center of the cylinder, T_i is the emplacement temperature of the conduit fill, T_{cr} is the ambient temperature of the country rock (i.e. volcanic edifice), a is cylinder radius (5 m), κ is the thermal diffusivity, and t is time (see Table 1 for units).

We model cooling of the tuffisite vein using a cooling model for an infinite sheet, following the equations for an infinite region with two boundary condition temperatures (equation (3), section 2.2, Carslaw and Jaeger, 1959):

$$T(t) = (T_i - T_{cr})\left\{\mathrm{erf}\left(\frac{b}{2\sqrt{(4\kappa t)}}\right)\right\} + T_{cr} \quad (2)$$

where T is the transient temperature at the center of the sheet, T_i is the emplacement temperature of the vein fill, and b is the half width of the tuffisite vein (0.05 m); all other parameters as defined above.

2.2.3. Input temperatures

Densification of pyroclastic deposits by viscous compaction is limited to temperatures above the glass transition temperature (T_g) (Grunder and Russell, 2005). The time interval for reaching T_g is predicted by our two thermal models (i.e. cylindrical conduit *vs.* narrow sheet) and depends on the initial temperature of the volcanic material, the temperature of the enclosing volcanic edifice and the material's thermal diffusivity.

The temperatures of volcanic edifices reported in the literature span from ambient near the surface to ~350 °C in large geothermal systems (e.g. Elders et al., 2014 and references therein). We choose 150 °C as the edifice temperature for the purposes of modeling. Eruptive temperatures of pyroclastic materials span ~700–1000 °C, as inferred by phase equilibria experiments, drilling, thermoremanent magnetization, and analyses of textures in ignimbrites (see e.g. Lesti et al., 2011; Rutherford et al., 1985 and references therein). For modeling purposes we assign 775 °C as the emplacement temperature of the pyroclastic material both in the conduit and the tuffisite veins. Higher initial temperatures for each environment result in longer cooling time to T_g, whereas cooler initial temperatures would result in shorter cooling times (see Appendix A3 for details).

2.3. Compaction modeling

2.3.1. Melt viscosity

Melt viscosity has been shown to exert the strongest control on the rate of porosity loss during welding and compaction (Farquharson et al., 2017b; Heap et al., 2014; Kolzenburg and Russell, 2014; Quane and Russell, 2005; Vasseur et al., 2013; Wadsworth et al., 2014). In our modeling, we adopt the high Fe-rhyolitic (i.e. tholeiitic) composition of Hrafntinnuhryggur, Krafla, Iceland, reported in Table A3 (Ryan et al., 2015; Tuffen et al., 2008). We allow for melt viscosity to vary as a function of both temperature and H_2O content. We assume that upon fragmentation the pore space in the pyroclastic conduit infill and tuffisite veins communicates with the atmosphere (i.e. they participate in outgassing). Based on this assumption we ascribe a conservative vapor overpressure of 1 MPa in the pyroclastic material. We model the temperature-dependent dissolved H_2O content using the solubility model of Liu et al. (2005). As H_2O solubility is inversely related to temperature (Liu et al., 2005; Ryan et al., 2015), the dissolved water content will increase during cooling, thereby reducing both the melt viscosity and T_g (Giordano et al., 2008). This expands and expanding the "welding window" – the temperature range where pyroclastic material densifies by viscous processes. We then use the model of Giordano et al. (2008) to quantify the transient melt viscosity and T_g as a function of temperature and the modeled transient H_2O content. The calculated melt viscosity is forwarded to the welding/compaction model.

2.3.2. Welding

We rearranged the welding equation developed by Russell and Quane (2005) to express explicitly the changes in porosity as the deposits cool and compact. This model is frequently used to examine the welding and compaction of viscous materials (Heap et al., 2015; Heap et al., 2014; Kolzenburg and Russell, 2014; Vasseur et al., 2013; Wadsworth et al., 2014).

Since welding and compaction occur in a confined environment, the volumetric strain (ε_v) can be attributed completely to the loss of porosity:

$$\varepsilon_v = \left(\frac{\Phi_0 - \Phi}{1 - \Phi}\right) \tag{3}$$

where Φ_0 is the initial porosity and Φ is the evolving porosity during compaction. Quane et al. (2009) modeled volumetric strain in the deposit as dependent on time, stress and melt viscosity with the relationship:

$$\boldsymbol{\varepsilon}_v = \left(\frac{1-\Phi_0}{\alpha}\right)\ln\left(\frac{\alpha\sigma\,\Delta t}{\eta_0(1-\Phi_0)} + e^{\frac{-\alpha\Phi_0}{1-\Phi_0}}\right) + \Phi_0 \tag{4}$$

where η_0 is the melt viscosity (Pa s), Δt the time difference between emplacement and the time of interest (s), σ the load stress in the deposit (Pa) and α is a dimensionless fitting parameter accounting for the textural heterogeneity of the compacting deposit. For welding of crystal-free glass fragments, α is 0.78 ± 0.15 (Quane et al., 2009). For crystal-bearing glass fragments this value is higher ($\alpha = 2.0$ Heap et al., 2014). Given that the crystal contents in tuffisite veins and pumices are generally low (Castro et al., 2012; Tuffen et al., 2003), we use 0.78 for α.

We set an initial porosity of 40% (i.e. a porosity fraction of 0.4) for our modeling, assuming that the particles are loosely packed during emplacement (Russell and Quane, 2005; Wright and Cashman, 2014) and assume an average dense rock equivalent density of 2500 kg/m^3. We model depths from 10 to 500 m. These are consistent with the shallow degassing regime where tuffisite veins are expected to be found (Heiken et al., 1988; Saubin et al., 2016; Stasiuk et al., 1996). The stress acting during compaction is calculated as a function of depth using the following formula:

$$\sigma = \rho g h \tag{5}$$

where σ is the load stress (Pa), ρ the deposit density (kg/m^3), g the gravitational acceleration and h the depth (m). For tuffisite veins we assume the overburden (i.e. the volcanic edifice) to have a constant bulk density of 2500 kg/m^3.

While pure compaction of conduit infill deposits would not increase the load at any given initial location in the deposit but merely reduce the height of the compacting deposit, it is commonly observed that volcanic domes form in the crater after explosive eruptions. Examples include the 1980 eruption of M. St. Helens (Swanson and Holcomb, 1990) or the 2300 BP eruption of Mt Meager (Hickson et al., 1999). The porosity loss is therefore compensated by rising material through the conduit, resulting in densification and an increase in load at a fixed depth. The stress acting on the conduit-filling deposits is therefore modeled as a function of depth and density of the overlying deposits, which increases during compaction as a function of the densification (i.e. porosity loss) of the overburden. We do not account for pore fluid pressure which may reduce the effective load on the compacting deposit. Therefore the resulting compaction timescales represent minimum values.

2.3.3. Permeability

The development of empirical models spanning a large range in permeability was initially hindered by the lower measurement limit of commercial permeameters, a limitation that has been addressed via custom built devices that enable measurements down to ~10^{-23} m^2 see Farquharson et al. (2015) and Kolzenburg et al. (2012) and references in both. A number of models describe the porosity-dependent permeability of volcanic fragmental materials (Heap et al., 2015; Klug and Cashman, 1996; Wadsworth et al., 2016; Wright and Cashman, 2014). These models are primarily empirical, and based on porosity and permeability measurements of natural materials or experimental products.

We have summarized these models in Fig. A1. All models have broadly the same shape, save the two-step evolution predicted by Heap et al. (2015). Because of the similarities in the way permeability decays with decreasing porosity, choosing one model over another changes the absolute permeability (Fig. A1A), but not the magnitude of permeability change (Fig. A1B). Here, we use the permeability (k) model presented by Wright and Cashman (2014) (red line in Fig. A1A):

$$k = 1.3 \times 10^{-21}\Phi^{5.2} \tag{6}$$

as it was fit to measurements from six naturally-occurring welded tuff deposits. Their model accounts for the change in porosity-dependent permeability as measured parallel to the welding/compaction fabric. This model has the advantage that it is simple, and does not include a grain size parameter. However, grain size can play and important role and varies drastically depending on the nature of and energy involved in the fragmentation process (Kolzenburg et al., 2013). Thus, if one were to know or assign a mono- or poly-disperse grain size distribution to a welding/compacting deposit, the model of Wadsworth et al. (2016) would be more suitable.

3. Results

3.1. Thermal evolution of volcanic outgassing systems

Figs. 2A and 2B summarize the thermal evolution of the two geometries: volcanic conduit and tuffisite vein, respectively. The

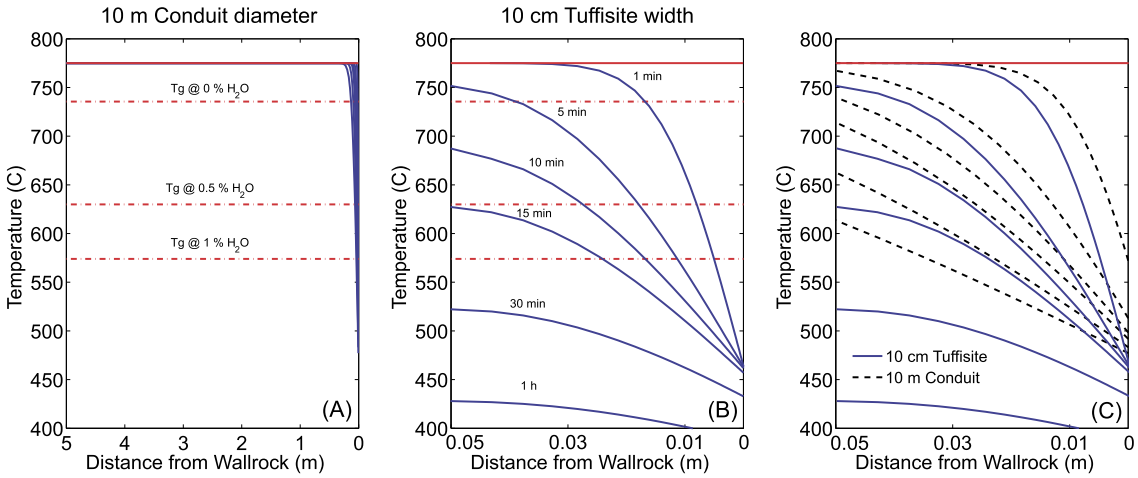

Fig. 2. Thermal evolution within the cooling deposits, plotted as half widths. Subplots A and B show the deposit temperature as a function of distance from the wall rock at time intervals between 1 min and 1 h. Subplot C shows a zoom in of the results of the thermal model as temperature *vs.* distance from the wall rock for the tuffisite vein (solid lines) and the conduit deposit (dotted lines) for times as in A and B.

model results demonstrate how the geometry and larger scale of the conduit, and the associated small surface to volume ratio, induces a large thermal inertia – most of the deposit remains near the emplacement temperature (T_i) over long timescales. Narrow tuffisite veins, on the other hand, have a greater surface to volume ratio. Therefore, the entire tuffisite vein volume cools rapidly, quenching to temperatures below T_g within minutes after emplacement.

When plotted at the same horizontal scale (Fig. 2C) it becomes apparent that, at the cooling interface, both models show a similar thermal evolution during the initial few minutes and only diverge with increasing time ($t > 15$ min). This is due to the large volume of conduit material, which increases thermal inertia and slows down cooling near the conduit wall. Over the same timescale, thin tuffisite veins cool quickly, quenching to below T_g in $t < 30$ min.

3.2. Porosity/permeability evolution during welding and compaction

Our model predicts porosity (subplots A and C) and permeability (subplots B and D) during compaction until $T = T_g$ or $\Phi = 0$ as a function of normalized location (i.e. margin *vs.* interior) within the deposit. The model results (Fig. 3) for tuffisites of 10 cm thickness and conduits of 10 m diameter show load stress (i.e. depth) to have a first order effect on the compaction efficiency in cooling deposits. Increasing load stress results in more efficient compaction – this effect is observed for both outgassing lithologies. However, as shown schematically in Fig. 3, while the center of tuffisite veins decreases in porosity with increasing depth, tuffisite margins always cool sufficiently fast to retain high porosities and permeabilities.

A comparison of the two outgassing deposit types shows that, for example, at 100 m burial depth ~90% of a 10 cm wide tuffisite vein remains at a permeability $>10^{-14}$ m^2. In contrast, at the same depth less than 1% of the cross section of a conduit of 10 m diameter remains above 10^{-14} m^2. This demonstrates that in conduit deposits only the zone in direct contact with the wall rock cools sufficiently fast to retain high porosity and permeability and that, once quenched, a single 10 cm wide tuffisite vein has the same outgassing capacity as the outermost 5–10 cm of a 10 m wide conduit.

3.3. Varying emplacement parameters

The thermal model (Fig. 2) shows that the cooling history is fundamentally dependent on the geometry and dimension of the deposit. Slow cooling in wide, cylindrical conduits supports intense welding and compaction whilst fast cooling of narrow, sheet like, veins suppresses welding and compaction intensity. Emplacement temperature also affects the rate and efficiency of the process, where a larger temperature differential between T_i and T_g creates a larger welding window and more intense welding. A detailed investigation of these parameters is presented in Figs. A2 and A3. The results show that increasing conduit diameter and tuffisite width, or emplacement temperature, decreases the fraction of the deposit that remains permeable, affecting the absolute cross-sectional area available to support outgassing. However, while changes in T_i and length scale (radius a or vein thickness b in equations (1) and (2), respectively) affect the absolute values of porosity and permeability for both deposit types, the relative changes and the resulting implications for the gas flow partitioning follow the same global pattern (see also Appendix A4).

4. Discussion

Results from our model simulations delineate the conditions whereby conduit margins and tuffisite veins are able to retain high porosity and permeability due to quenching. Yet, our results suggest that tuffisites hosted within the cool edifice retain higher porosities and permeabilities than measured for tuffisites hosted in the magma (Kendrick et al., 2016; Kolzenburg et al., 2012; Saubin et al., 2016; Tuffen et al., 2003). In the following sections we show how seemingly contradictory observations on 1) long timescales of tuffisites as active gas pathways recorded in geochemical signatures (Berlo et al., 2013; Paisley et al., 2019; Saubin et al., 2016) and 2) short timescales of permeability annihilation in tuffisites proposed by experimental and modeling efforts, fit into a unified conceptual model by accounting for its non-isothermal nature. Finally, we outline the potential use of these insights as a new monitoring approach for active volcanoes that typically produce Vulcanian to Sub-Plinian eruptions.

For the purpose of this model we assume cylindrical conduits and sheet-like tuffisite veins (See section 2.2.1). As such, the model results represent local cross sections through the deposit and the model results remain valid also for funnel shaped conduits (at the location where the respective modeled diameter is present). However, since the quench effect is restricted to the outermost portion of the conduit in contact with the country rock (~10–60 cm, depending on emplacement temperature, depth and deposit dimension; see also Appendix A3), the absolute diameter of the conduit has little influence on compaction efficiency of the remainder of

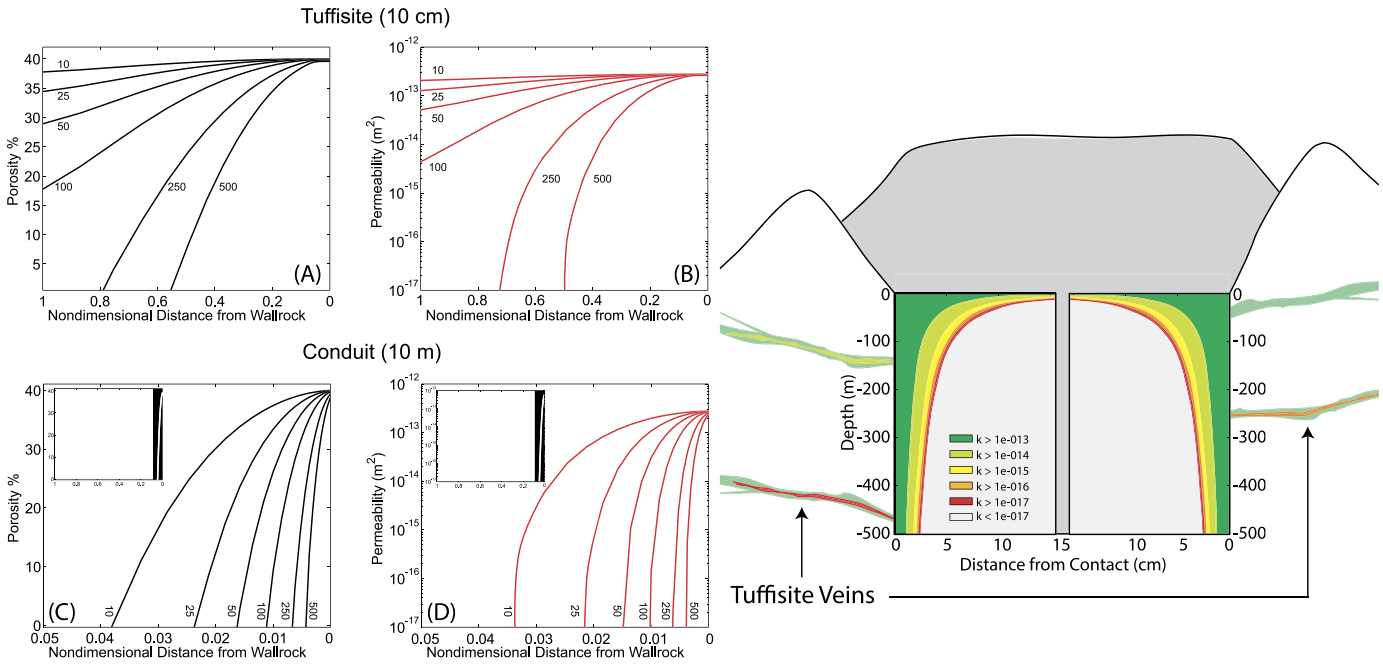

Fig. 3. Summary of the model results showing the quenched-in physical properties of the deposit upon cessation of welding and compaction, contoured for varying emplacement depths (contours). Subplots A and B show the porosity and permeability of compacting tuffisite veins of 10 cm width, as a function of distance from the wall rock (0 being the contact to the wall rock and 1 being the center of the cooling deposit). Subplots C and D show the porosity and permeability of compacting conduit deposits of 10 m diameter. Note the narrow normalized distances (0 to 0.05; i.e. the outer 25 cm of the conduit infill closest to the wall rock interface) for subplots C and D. Insets shows the area enlarged in subplots C and D. The cartoon shows maps of the results for conduit permeability over depth and distance from the wall rock contact. For better readability, results are plotted for the outer 15% of the conduit only. Tuffisite permeability maps are shown schematically. Independent of the emplacement depth, a high permeability quench margin remains at the contact between the vein and the host rock, whereas the center of the vein reaches lower permeabilities with increasing depth. (For interpretation of the colors in the figure(s), the reader is referred to the web version of this article.)

the deposit. The same applies for non-horizontal tuffisite veins. If one were to try to understand the degassing behavior of an entire tuffisite vein from depth to surface, the critical parameter would be the depth at which it taps a gas reservoir, rather than its orientation. This is because the outgassing capacity of a vein is limited by the maximum depth at which it intersects the reservoir, since compaction efficiency is positively correlated with depth (i.e. at depth, porosity and permeability will be lower than if the vein taps the gas reservoir at a shallower levels).

4.1. Outgassing lithologies in their natural habitat

The extreme margins of conduits are infrequently exposed but, where available, field observations, including outgassing patterns (Holland et al., 2011; Lavallée et al., 2012) and porosity and permeability values as well as alterations in the margins of dissected conduits or bore holes (Cloos, 1941; Heiken et al., 1988; Stasiuk et al., 1996), show the margins of volcanic conduits to operate as long-lived outgassing pathways. Similarly, where exposed in situ, tuffisites are commonly poorly welded and display high porosities and high permeabilities (Cloos, 1941; Heiken et al., 1988; Stasiuk et al., 1996).

These observations are in good agreement with our model results, which predict tuffisite veins to have high porosities and permeabilities. However, they are at odds with the numerous studies that describe densely welded (Berlo et al., 2013; Castro et al., 2012; Heap et al., 2015; Kendrick et al., 2016; Saubin et al., 2016; Tuffen et al., 2003) or otherwise lithified (Farquharson et al., 2015; Kolzenburg et al., 2012) low porosity/permeability tuffisites recovered from deposits of explosive eruptions. These dense materials have been interpreted as representative of the character of tuffisite veins in the subsurface. As a result, experimental studies (Heap et al., 2015, 2014; Kolzenburg and Russell, 2014; Vasseur et al., 2013; Wadsworth et al., 2014, 2016), empirical studies on natural materials ((Farquharson et al., 2015; Gardner et al., 2018; Kendrick et al., 2016; Kolzenburg et al., 2012; Quane and Russell, 2003), 2005; Rust and Cashman, 2004; Wright and Cashman, 2014) and numerical models (Chevalier et al., 2017; Farquharson et al., 2017b) have sought to understand the conditions that generate their microstructures and low final porosities and permeabilities.

We can resolve the apparent discrepancy between the higher porosity of tuffisites found in situ and suggested by our model, and the observation of low porosity tuffisites in pyroclastic deposits by considering their respective strengths: an increase in porosity is accompanied by a marked decrease in coherence and rock strength (see for example Quane and Russell (2003), Kolzenburg et al. (2012) and Heap et al. (2015)). The low coherence of highly porous materials suggests a lower likelihood that the material will remain intact during an eruption, and thus a lower potential for being preserved in ejected blocks. Thus, the apparent discrepancy between our model results and tuffisite veins reported in the literature may reflect a sampling bias where only the strongest tuffisite blocks, having lower porosity and permeability values, are preserved during eruption. Many tuffisites described in the current literature are therefore likely not representative of pathways contributing to magma outgassing but represent the most evolved/completed end-members of the welding and compaction process that are strong enough to survive an eruption i.e. “the ones who got away”.

4.2. Tuffisite longevity

Our model results show that both tuffisite veins and conduit margins are likely to “freeze in” high porosity and permeability, and to act as long-lived outgassing pathways. These compaction timescales appear at odds with the current understanding of the lifespan of tuffisites as permeable pathways (Chevalier et al., 2017; Farquharson et al., 2017b; Gardner et al., 2018; Kendrick et al., 2016; Kolzenburg et al., 2012; Rust and Cashman, 2004). However, previous studies (Table A2 and section 4.1) have focused

on tuffisite veins that intrude the hot conduit-infilling deposits (lava or pyroclastic deposits) where temperatures are maintained, compaction is rapid, and permeability networks are short lived (Heap et al., 2015; Quane and Russell, 2005; Quane et al., 2009; Vasseur et al., 2013; Wadsworth et al., 2016). As an example, Chevalier et al. (2017) and Farquharson et al. (2017b) model the decrease of porosity and permeable gas loss at the conduit-wall rock interface during dome growth and loading of the edifice, and report significant permeability loss on the timescale of tens of minutes to hours. Similarly, Quane and Russell (2005) and Wadsworth et al. (2014) present experimental data on the densification of analogue and natural materials and give densification timescales of tens of minutes to hours when the material viscosity is sufficiently low both under a normal load and when compacting by surface tension alone. This is echoed also in a recent study by Gardner et al. (2018) that expanded the experimental conditions to elevated hydrostatic pressure and hydrous conditions, resulting in a decrease in melt viscosity and even faster densification ($<<1$ h). These timescales would decrease even further under a load stress.

However, we show here that the compaction history of hot ($>T_g$) tuffisite veins injected into the cooler edifice or wall rocks (25–350 °C) is very different from the conditions assumed in the aforementioned studies. Modeling the permeability loss due to compaction as tuffisite veins cool against cool host rocks (i.e. $<<<$ T_g) allows to explain the preservation of long-lived outgassing structures resulting from "freezing in" porosity and permeability. Our results show that for any reasonable assumption of environmental conditions, this quench effect occurs on timescales shorter than the welding and compaction timescale, allowing for porosity and permeability retention. This suggests that tuffisites in the subsurface are significantly more porous and permeable and therewith remain active outgassing features for longer timescales than previously thought.

4.3. Implications for the observed gas flow budget at explosive volcanoes

Our results show that both tuffisite veins and conduit margins can "freeze in" high values of porosity and permeability thereby preserving long-lived outgassing pathways. Fig. 3 highlights that tuffisite veins possess quenched margins even at deep levels in the volcano. These intersect, and therewith tap, the compacting conduit infill as well as potentially existing deeper pockets of permeable, foamed magma and may thus represent effective outgassing pathways. In order to assess the balance between the outgassing capacities of the two lithologies, we calculate the area within each deposit that remains above the average edifice permeability. As an example we compare the permeability evolution of a 10 m diameter conduit and a 10 cm thick tuffisite for an emplacement temperature of 775 °C. Since welding is dependent on the load acting during compaction, we evaluate the outgassing capacity at a fixed depth of 100 m for this example.

Estimation of tuffisite frequency and proportion in the subsurface are tricky and literature values that are based on fracture density distributions and/or drill core fracture spacing vary drastically. They range from 25% in Farquharson et al. (2017b), over 10–15% in Heiken et al. (1988), down to 0.2% in Goto et al. (2008). Here we take a conservative approach and assume that during an eruption ~5% of the conduit volume is converted to tuffisite veins within the surrounding wall rocks. Initially, therefore, the permeable, high porosity horizontal cross section of the 10 m diameter conduit equals 78.54 m^2 and that of the tuffisite vein equals 3.93 m^2. For a tuffisite vein of 10 cm thickness, this translates to a width of ~40 m. These dimensions are in agreement with estimates and textural work on tuffisite veins originating from shallow (10–300 m depth) dome forming eruptions (Stasiuk et al., 1996; Tuffen et al., 2003) as well as tuffisites associated with basaltic diatremes (Cloos, 1941).

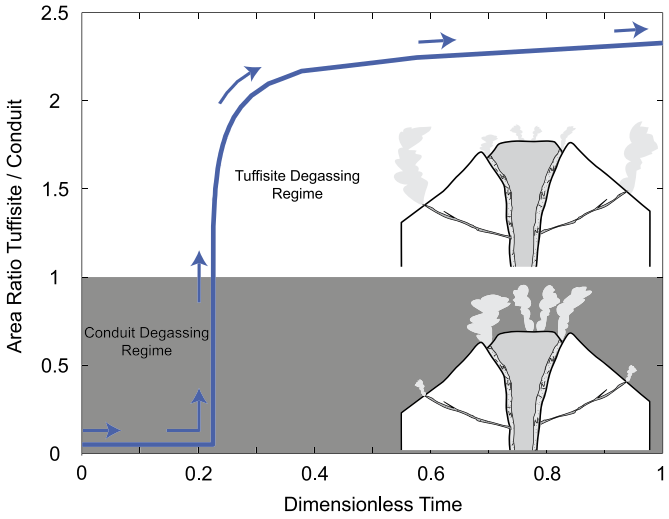

Fig. 4. Summary of the model results showing the evolution of the outgassing capacity (i.e. the ratio of permeable areas ($k > 10^{-16}$ m^2)) as a function of dimensionless time (i.e. absolute time normalized to the time required to quench to T_g). The plot shows the results for a 10 m conduit diameter and a 10 cm tuffisite vein, both at 100 m depth.

In order for gas escape to be controlled by the conduit or the tuffisite network, the permeability of the respective deposit must be higher than both the host wall rocks and the magma column, which are generally below 10^{-16} to 10^{-17} m^2 (see Farquharson et al. (2015) and references therein). To assess the relative importance of the two outgassing lithologies we assign a threshold of 10^{-16} m^2 – for permeabilities above this value, gas escape is concentrated within the respective deposit; for lower permeabilities, outgassing has no preferred pathway and occurs pervasively through the volcanic edifice. This threshold value is supported the work of Collinson and Neuberg (2012) who model time dependent variations in pressure based on Darcy's law and find that systems below 10^{-16} m^2 behave as effectively sealed systems. Based on their model they assign this value as the threshold between "open" and "closed" system outgassing.

The contribution of the respective deposit to system-wide outgassing is evaluated by calculating the area of the tuffisite and conduit deposits that remains above the permeability threshold of 10^{-16} m^2 as a function of time. Then we calculate the ratio of these areas: a ratio of <1 indicates a larger gas flow capacity (i.e. cross sectional area available for outgassing) in the conduit infill, whereas a ratio of >1 indicates that there is higher gas flow capacity in the tuffisite. Using this ratio we can reconstruct the relative contribution to outgassing of these two types of deposit throughout the welding and compaction processes, until the point where final porosities and permeabilities are "frozen in" (Fig. 4).

Seconds after emplacement both the conduit and tuffisite veins have permeabilities $>>10^{-16}$ m^2. Because of the greater area available for outgassing in the conduit, the ratio between the tuffisite to conduit permeable area is very small, and gas flow will dominantly be focused within the conduit. However, due to the high thermal inertia of the conduit geometry, the central parts of the conduit remain hot and quasi-isothermal (see Fig. 2). As a result, compaction within the conduit infill is very efficient, and permeability rapidly decreases below 10^{-16} m^2 for the largest part of the conduit, leaving only a narrow permeable annulus at the contact with the host rock. This rapid permeability reduction in the conduit is not mirrored in the tuffisite veins because of their fast cooling rate (Figs. 2 and 3). Therefore, as compaction proceeds, the system-wide permeable outgassing area ratio becomes >1; i.e.

outgassing is focused within the tuffisite vein system. This is expressed in the model results as an almost instantaneous change in the outgassing area ratio (Fig. 4). After this point, the majority of the conduit is effectively re-sealed and quenched tuffisite veins act as the primary outgassing pathways. In summary, Fig. 4 shows that the outgassing potential of each deposit will undergo a characteristic evolution that is dictated by the geometry and dimension dependent variation in cooling history of the tuffisite veins and conduit. An analysis of variations in vein geometry on this outgassing budget is presented in Appendix A4 and shows that this outgassing pattern remains unchanged for any reasonable vein size.

Small changes in the capacity of a volcanic system to dissipate overpressure via outgassing can bring forth dramatic changes in eruption style (explosive *vs*. effusive) and drive instabilities in the eruption regime e.g. Jaupart and Allègre (1991). Thus our model for an evolving outgassing budget may yield information on critical changes in the physical state of a volcanic system that are not detectable via currently available monitoring approaches.

5. Potential use as a low cost monitoring tool

Our results show that tuffisite veins in the volcanic edifice may retain high permeabilities over long timescales relative to the compacting conduit, and that they can become the dominant contributor to magma outgassing at relatively short times after eruption. This temporal evolution in outgassing behavior (shift from conduit- to tuffisite-dominated outgassing) has been suggested by field measurements, for example during SO_2 outgassing at Soufrière Hills volcano (Edmonds et al., 2003): the authors observe decreases in SO_2 flux over three orders of magnitude, which they link to permeability changes on two different timescales 1) slow and long term permeability decrease from July 1998 to November 1999 that they attribute to precipitation of hydrothermal minerals, as also suggested by for example Taran et al. (2001) and 2) rapid increase of permeability during the production of pyroclastic flows followed by fast (timescales of minutes to hours) permeability reduction in the upper conduit and dome due to cooling and "sealing". Sealing of the upper conduit and dome results in gas getting trapped within closed fractures, priming the next pyroclastic event. This indicates that outgassing patterns may inform on densification and permeability-reduction occurring within volcanic edifices. On this basis we see the potential for a new monitoring strategy to assess the development of gas overpressures and potential onset of explosive activity.

As shown above, the redistribution of gas flow between conduit and tuffisites is a result of their geometry-dependent quench efficiency. This time dependency in the outgassing capacity of the two deposit suggests that changes in the activity and total flux rates of distal fumaroles may inform on the pressure-state of a volcano. Immediately after an eruption, the high gas flow capacity of the conduit will result in little to no gas flow through the tuffisite-linked fumarole network. With time though the conduit infill deposits will densify, and the outgassing capacity of tuffisites will rapidly exceed that of the conduit (Fig. 4). At this point, fumaroles linked to these tuffisites they will resume their activity. Any change in the pressure state of the volcano will then be directly reflected in the volume of gas flux from these fumaroles (i.e. an increase in gas pressure within the conduit will result in higher flux, and vice versa) making the total gas volume expelled via these fumaroles a direct indicator of the pressure evolution within the edifice.

We suggest this hypothesis could be tested in the field, where records of fumarole activity and eruptive activity can be linked. We propose several locations where this work may be informative:

- Santiaguito, Guatemala, where small explosive eruptions are frequent and can be readily monitored and correlated to the temporal evolution of flow rates of fumaroles.
- Colima, Mexico, where Vulcanian style eruptions are frequent and a wealth of monitoring procedures is in place that include data on the dome/crater activity and fumarole activity.
- Tungurahua, Equador, where gas-particle intrusions in the edifice have been identified previously (Molina et al., 2004) and gas monitoring equipment could be added with reasonable effort.
- Turrialba, Costa Rica, where automated video monitoring for crater outgassing is in place and monitoring sites for fumaroles could be added with limited effort.
- Sabancaya, Peru, where small explosive eruptions occur every few hours and automated video monitoring of the edifice is in place.
- Mount Agung, Indonesia, where Vulcanian style eruptions started recently and monitoring sites at advantageous vantage points could be added with reasonable effort.

This strategy (monitoring the activity of or, ideally, total flux of fumaroles) could potentially be employed as a low cost pressure monitoring tool, which would be of great benefit to communities where the financial capacity for sophisticated instrumentation such as seismometers, tilt-meters or infrasound recorders is limited.

6. Conclusions

Results from our modeling suggest the following conclusions:

1. The differences in geometry and dimensions between the two dominant outgassing pathways (conduit infill *vs*. tuffisite veins) result in drastically different post eruptive cooling paths, creating characteristic patterns of compaction and permeability loss.
2. The thermal evolution of the outgassing system during welding and compaction is of paramount importance for the efficiency of permeability retention.
3. The timescales for porosity loss in both outgassing systems are highly dependent on the evolution of the bulk rheology of the deposit (governed by melt composition and cooling history).
4. The switch from conduit-dominated outgassing to tuffisite-dominated outgassing occurs abruptly once the bulk of the conduit filling deposit has reached permeability values below the edifice forming rocks (commonly $<10^{-16}$ m^2), and will be reflected in the activity/total flux from tuffisite-fumaroles.
5. This characteristic evolution of post eruptive gas flow has the potential to be used for low cost monitoring of permeability shut-off and the onset of pressurization of explosive volcanoes.

Acknowledgements

S. Kolzenburg acknowledges the support of a H2020 Marie Skłodowska-Curie Actions fellowship DYNAVOLC – No. 795044. J.K. Russell acknowledges an Natural Sciences and Engineering Research Council of Canada Discovery grant number: RGPIN-2018-03841. The constructive comments of Heather Wright, Hugh Tuffen and Tamsin Mather helped us improve the quality of this manuscript.

Appendix A1. Overview of available permeability models

There are a number of models that describe the porosity-dependent permeability of volcanic fragmental materials (Heap et al., 2015; Klug and Cashman, 1996; Sparks et al., 1999; Wadsworth et al., 2016; Wright and Cashman, 2014; Burgisser et al., 2017;

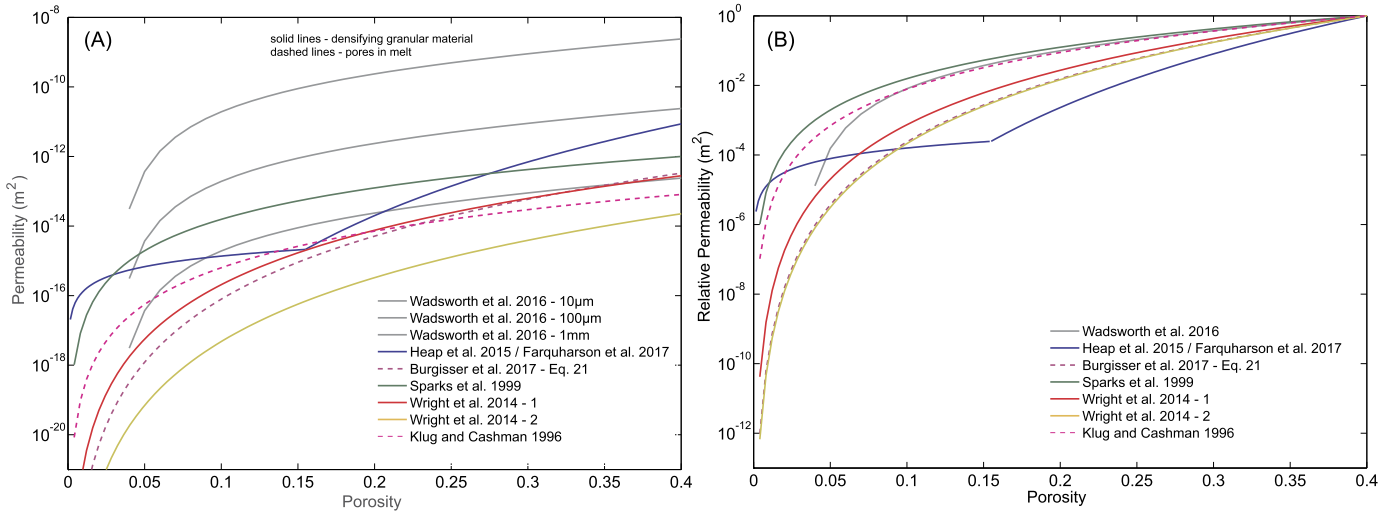

Fig. A1. Available permeability models. (A) Models vary in the predicted absolute permeability values by several orders of magnitude, but show a broadly similar shape. The two-step evolution of the model presented in (Heap et al., 2014) is a result of the identification of a changepoint in this relationship. (B) The dependence of relative permeability (ratio of modeled permeability at a given porosity to the modeled permeability at 0.40 porosity) to porosity does not change significantly between individual models.

Farquharson et al., 2017a). These models are primarily empirical, and based on the measured porosity and permeability of natural materials or experimental products; they are summarized in Fig. A1. All models have broadly the same shape, save the two-step evolution presented by Heap et al. (2015). Because of the similarities in the way permeability decays with decreasing porosity, choosing one model over another changes the absolute permeability (Fig. A1A), but does not significantly change the relative permeability (permeability at a modeled porosity ratioed to the permeability at the initial porosity) (Fig. A1B). For our modeling purposes we have therefore selected the model of Wright and Cashman (2014) – equation (6) in this manuscript, that describes the porosity-permeability relationship for gas flow along the foliation of porous volcanic rocks. This model represents the best approximation of the average relative permeability of all models (red line in Fig. A1).

Table A1
Compilation of existing conduit diameter measurements.

Volcano	Diameter (m)	Lithology	Reference
Chaitén, Chile	20–50	Rhyolite	Browne and Szramek, 2015
Chaitén, Chile	10–100	Rhyolite	Castro and Dingwell, 2009
Colima, Mexico	50	Andesite	Lavallée et al., 2012
Cordon Caulle, Chile	50	Rhyolite	Schipper et al., 2013
Etna, Italy	25	Trachybasalt	Rymer et al., 1993
Mt. Meager, Canada	40–45	Dacite	Campbell et al., 2013
Mt. St. Helens, USA	20 ± 5	Dacite	Barmin et al., 2002; Rutherford and Hill, 1993; Swanson and Holcomb, 1990
Mt. St. Helens, USA	40	Dacite	Chadwick et al., 1988
Mt. St. Helens, USA	150–200	Dacite	Vallance et al., 2008; Schneider et al., 2012
NW Rota-1 Mariana Arc	<15	Basaltic-Andesite	Embley et al., 2006; Walker et al., 2008; Butterfield et al., 2011; Deardorff et al., 2011
Paracutin, Mexico	10	Basalt	Vespermann and Schmincke, 2000
Santiaguito, Guatemala	150	Dacite	Head et al., 2003
Santiaguito, Guatemala	36	Dacite	Holland et al., 2011
Santiaguito, Guatemala	50	Dacite	Bluth and Rose, 2004
Soufrière Hills, Montserrat	30	Andesite	Browne and Szramek, 2015
Soufrière Hills, Montserrat	50–60	Andesite	Watts et al., 2002
Soufrière Hills, Montserrat	30–50	Andesite	Sparks et al., 2000
Tavurcur, New Guinea	100	Dacite	McNutt et al., 2015
Vesuvius, Italy	65	Tephrite	Shea et al., 2011
Vesuvius, Italy	80–90	Tephrite	Macedonio et al., 2008
Mule Creek, USA	50	Rhyolite	Stasiuk et al., 1996
Shiotani, Japan	>1 km	Rhyolite	Kano et al., 1997
Generic Explosive	20	N/A	Neuberg, 2000
Generic Vulkanian	30	N/A	Melnik and Sparks, 1999; Costa et al., 2007; Delany and Pollard, 1981; Clarke et al., 2015
Generic Explosive	50	N/A	Mangan et al., 2004; Caricchi et al., 2007
Generic Explosive	100	N/A	Neri and Dobran, 1994
Generic Explosive	127	N/A	Papale, 1999
Generic Explosive	10–50	N/A	Bonaccorso and Davis, 1999; De Michieli Vitturi et al., 2008
Generic Explosive	50–90	N/A	Jellineck and Bercovici, 2011
Generic Explosive	20–40	N/A	Gonnermann and Manga, 2003
Generic Explosive	20–100	N/A	Wilson et al., 1980
Generic Plinian	10–15	N/A	Carey and Sigurdsson, 1989

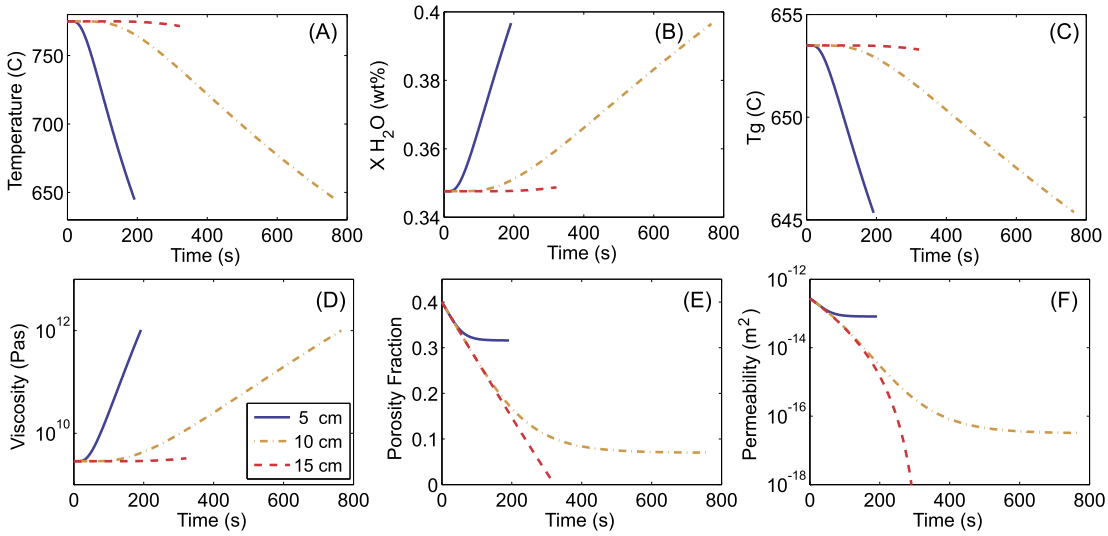

Fig. A2. Examples of the temporal evolution of the model parameters. Subplots A, B, C, D, E and F show the temporal evolution of temperature, dissolved water content, T_g, viscosity, porosity fraction and permeability, respectively. Results are plotted for tuffisite thicknesses of 5, 10 and 10 cm width as solid, dash dotted and dashed lines, respectively. Note that the 15 cm vein is compaction limited (i.e. complete porosity loss prior to reaching T_g) whereas the 10 and 5 cm veins are cooling limited (i.e. T_g is reached before complete porosity loss, quenching in a permeable texture).

Appendix A2. Temporal evolution of all model parameters during compaction

A2.1. Conduit geometry

Due to the large thermal buffering capacity of the material in the interior of a conduit (see thermal evolution of a cooling conduit in Fig. A2 in the main text), the non-isothermal area, relevant for permeability retention, is a narrow region of the deposit near the conduit wall. Since anything beyond this non-isothermal zone cools so slowly that porosity is annihilated before reaching T_g, variations in the conduit diameter do not affect the model results of porosity and permeability evolution across this contact zone significantly. Therefore, an increase in conduit diameter results in an overall increase in the area of the permeable annulus in contact with the conduit wall but not the evolution of its physical properties. Since we assume that in any modeled scenarios, the cross sectional area of tuffisites created during eruption is 5% of the cross sectional area of the conduit, the area ratio (Fig. 4 and Fig. A5) remains unaffected by conduit geometry.

A2.2. Tuffisite geometry

Contrary to the conduit infill deposit, dimension plays an important role in the evolution of the physical properties of tuffisites. In order to evaluate the significance of the change in compaction efficiency, we ran our model using varying tuffisite widths (within the range expected in nature) and assess how this controls the model results: In Fig. A2 we plot each of the model parameters (i.e. thermal, transport and physical properties) against time. The data show the contemporaneous model parameter evolution throughout the compaction process in three tuffisite veins from initial emplacement to the point where the process stalls (i.e. $T \leq T_g$ or $\Phi = 0$). Results are plotted for the following model parameters: thickness: 5, 10 and 15 cm; $T_i = 775\,^{\circ}\mathrm{C}$; pore pressure 1 MPa; $\Phi_0 = 0.4$; depth = 150 m; location: center of the compacting vein (i.e. 2.5, 5 and 7.5 cm from the wall rock contact).

This analysis demonstrates the interdependence of model parameters. Compaction in the center of both the 5 and 10 cm thick veins is cooling limited (i.e. the process reaches T_g), quenching in a porosity of 35% and 7%, and a permeability of 8×10^{-14} m^2

Table A2
Compilation of existing tuffisite thickness measurements and locations.

Volcano	Thickness (m)	Lithology	Reference
Chaiten, Chile	<0.1	Obsidian $\Phi < 0.1$	Saubin et al., 2016
Chaiten, Chile	<0.03	Obsidian $\Phi < 0.1$	Castro et al., 2012
Colima, Mexico	0.003–0.05	Andesite $\Phi > 0.8$	Kolzenburg et al., 2012
Colima, Mexico	0.02	Andesite $\Phi > 0.8$	Heap et al., 2015
Colima, Mexico	0.001–0.01	Andesite $\Phi > 0.8$	Farquharson et al., 2016
Colima, Mexico	0.001–0.03	Andesite $\Phi > 0.8$	Kendrick et al., 2016
Cordon Caulle, Chile	<0.5	Obsidian $\Phi < 0.1$	Schipper et al., 2013
Inyo Domes, USA	0.07–0.4	Rhyodacite $\Phi < 0.78$	Heiken et al., 1988
Mono Craters, USA	0.001–0.02	Obsidian $\Phi < 0.1$	Rust and Cashman, 2004
Mule Creek, USA	0.001–0.05	Rhyolite $\Phi < 0.1$	Stasiuk et al., 1996
Rocche Rosse, Italy	0.001–0.5	Obsidian $\Phi < 0.1$	Cabrera et al., 2015
Rocche Rosse, Italy	0.03–0.1	Obsidian $\Phi < 0.1$	Cabrera et al., 2011
Schwaebische Alp, Germany	<0.7	Basalt $\Phi < 0.9$	Cloos, 1941
Torfajokull, Iceland	0.001–0.01	Obsidian $\Phi < 0.1$	Tuffen et al., 2003
Torfajokull, Iceland	0.001–0.05	Obsidian $\Phi < 0.1$	Tuffen and Dingwell, 2004
Torfajokull, Iceland	0.013–0.05	Obsidian $\Phi < 0.1$	Berlo et al., 2013
Torfajokull, Iceland	0.001–0.02	Obsidian $\Phi < 0.1$	McGowan et al., 2016
Unzen, Japan	0.035	Dacite $\Phi > 0.6$	Farquharson et al., 2017b
Unzen, Japan	<0.25	Dacite $\Phi > 0.6$	Goto et al., 2008

Φ Values indicate the volume fraction of non glassy material in the respective deposit.

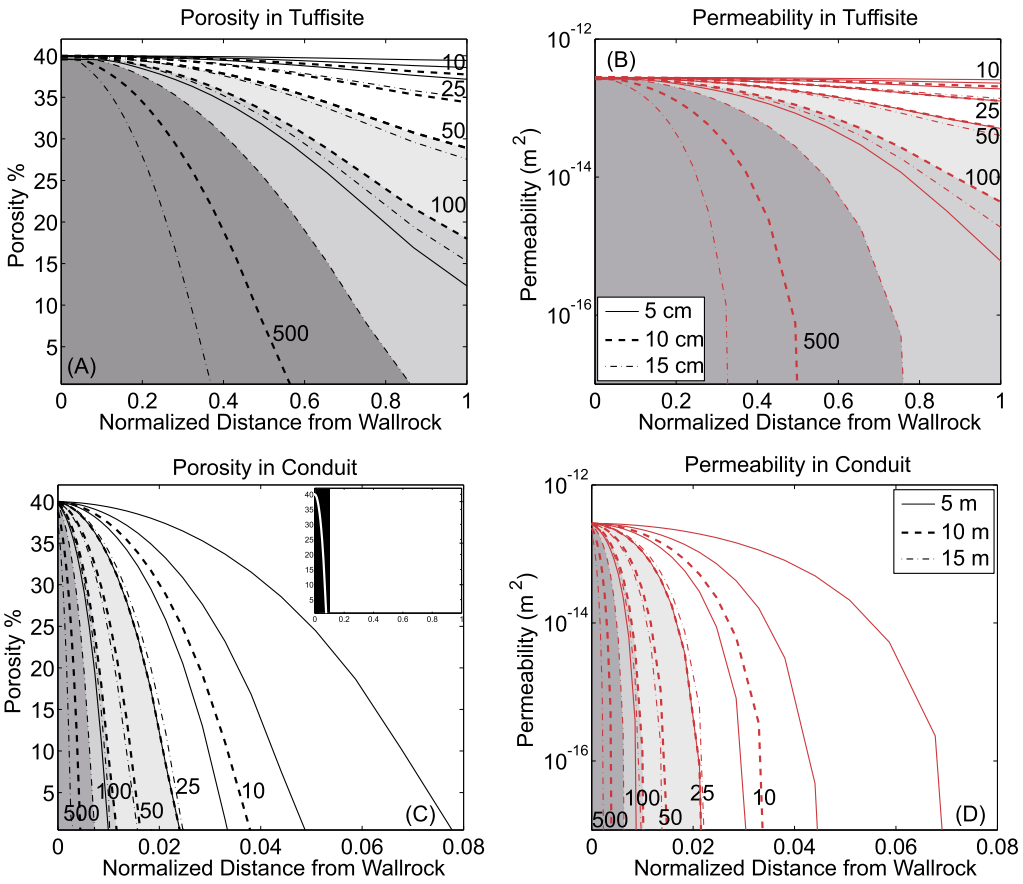

Fig. A3. Summary of the model results showing the quenched in physical state of the deposit upon cessation of welding and compaction for varying deposit geometries (line style) and emplacement depth (labels). Subplots A and B show the porosity and permeability of compacting tuffisite veins of 5 (solid lines), 10 (dashed lines), and 15 (dash dotted lines) cm width, as a function of distance from the wall rock, respectively. Subplots C and D show the porosity and permeability of compacting conduit deposits of 5 (solid lines), 10 (dashed lines), and 15 (dash dotted lines) m diameter, as a function of distance from the wall rock, respectively. Shaded areas highlight the fields for each geometry at 100 m burial depth. Note that due to the relatively small volume of material that is able to retain porosity and permeability after compaction the X-axis for the model results of compacting conduits is only shown for normalized distances of 0 to 0.08. The small insert in subplot C shows the area enlarged in subplots C and D.

and 3×10^{-17} m^2 for the 5 and 10 cm vein center, respectively. Compaction in the center of the 15 cm thick vein is complete (i.e. Φ reaches 0), rendering the center of the vein impermeable, before significant cooling occurs. However, the outer 10 cm of the 15 cm vein that are in contact with the wall rock are cooling limited and retain permeability. In the following section we present the model results at the point of cessation of compaction (i.e. the final Φ and k that are quenched in upon reaching T_g).

Appendix A3. The effect of changing process parameters

Due to the large parameter variation we present the model results incrementally in the following sub sections, investigating the effect of each parameter on the efficiency of cooling and permeability retention separately. We start by showing the effect of deposit geometry, varying with depth, and proceed to discuss the effect of varying emplacement temperatures.

A3.1. The effect cooling geometry and dimension

Fig. A3 shows the modeled porosity (subplots A and C) and permeability (subplots B and D) at the end of compaction (i.e. where $T = T_g$ or $\Phi = 0$) as a function of location within the deposit for tuffisites of 5, 10 and 15 cm thickness and conduits of 5, 10 and 15 m diameter. Results are reported as absolute values for porosity and permeability, whereas the location in the deposit is plotted as normalized distance between the center of the vein or conduit and the contact to the wall rock, 0 being the contact, and 1 being the center of the respective deposit.

Table A3
Major element (anhydrous) composition of obsidian from Hrafntinnuhryggur, Krafla, Iceland from Tuffen et al. (2008).

Oxide	Wt% oxide
SiO_2	75.23
TiO_2	0.23
Al_2O_3	12.00
FeO(t)	3.28
MnO	0.11
MgO	0.10
CaO	1.66
Na_2O	4.15
K_2O	2.75
P_2O_5	0.00
Analytical total	99.51

The model results show that both depth (controlling the load stress) and deposit geometry (controlling the cooling efficiency) have first order effects on the compaction efficiency in cooling deposits. Increasing load stress results in more efficient compaction – this effect is observed for both geometries. For tuffisite veins, an increase in vein width results in slower cooling and, therewith, more efficient compaction, resulting in decreasing porosity and permeability with increasing distance from the wall rock (i.e. the cooling surface). For conduit deposits, only the zone in direct contact with the wall rock is cooling sufficiently rapidly to

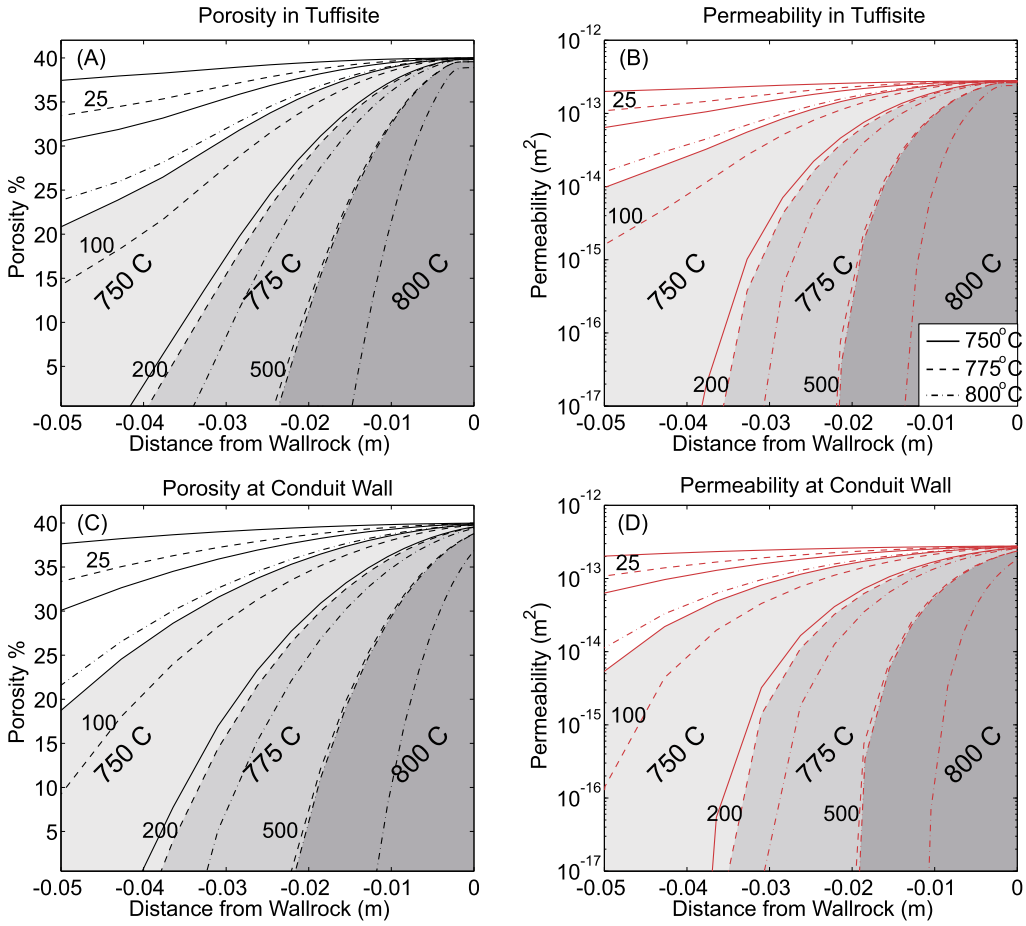

Fig. A4. Summary of the model results showing the quenched in physical properties of the deposit upon cessation of welding and compaction for a 10 cm tuffisite width (subplots A and B) and a 10 m conduit diameter (subplots C and D) as a function of distance from the wall rock. Solid, dashed and dot-dashed lines represent the model results for 750, 775 and 800 °C, respectively. Data are plotted for 25, 100, 200 and 500 m depth for all three emplacement temperatures. Small numbers label depth contours for emplacement at 775 °C. Light, medium and dark grey fields highlight the quenched in state at 200 m depth for emplacement temperatures of 750, 775 and 800 °C, respectively.

quench in porosity and permeability. In contrast to tuffisite weins, the largest part of the deposit remains at temperatures above T_g for sufficient time to result in complete compaction and porosity/permeability loss. Albeit increasing in conduit diameter results in a decrease in the fraction of the conduit cross section that remains permeable, the absolute outgassing area increases. At 100 m burial depth, for example, ~90% of a 10 cm wide tuffisite vein (medium grey shaded areas in A and B) remain at a permeability above 10^{-14} m^2, whereas for a conduit of 10 m diameter (medium grey shaded areas in C and D) less than 1% of the cross section remain above 10^{-14} m^2.

A3.2. The effect of emplacement temperature

To investigate the effect of emplacement temperature on the quench efficiency and porosity and permeability retention we plot the model results upon cessation of compaction for 10 cm tuffisite width and 10 m conduit diameter at emplacement temperatures of 750, 775 and 800 °C for shallow (25 m), intermediate (100 m and 200 m) and deep (500 m) emplacement scenarios (Fig. A4). The results show that for both tuffisite veins and conduit walls, emplacement temperature has a first order effect on the efficiency of porosity and permeability loss, where increasing emplacement temperatures results in more efficient compaction and, therewith, decreasing porosity and permeability for any given location within the deposit.

The model results highlight that, in cross section, a single tuffisite vein of 10 cm width retains the same outgassing capacity as the margin (outermost 5–10 cm) of a conduit of 10 m diameter upon quenching. The data show that the absolute differences in permeability and porosity quenched in directly at the conduit margin and across the tuffisite vein are relatively small. The conduit wall cools somewhat slower and therefore, compaction is slightly more efficiently, especially in locations deeper in the conduit. This results in a slightly narrower zone of high porosity and permeability at the conduit wall than at the contact between tuffisite and host rock. The data show further that the absolute differences in permeability and porosity quenched in directly at the conduit margin and across the tuffisite vein are relatively small.

Appendix A4. The effect of tuffisite width on the gas flow budget during outgassing

As outlined in Appendix A2, the area relevant for permeability retention in conduit infill encompasses only the outermost fractions of the deposit near the conduit wall, and variations in the conduit diameter do not affect the model results of porosity and permeability evolution across this contact zone significantly. An increase in conduit diameter results in an increase in the area of this permeable annulus and could, with that, influence the outgassing budget. However, since we assume that the cross sectional area of tuffisites is 5% of the cross sectional area of the conduit, the area ratio remains unaffected by conduit geometry.

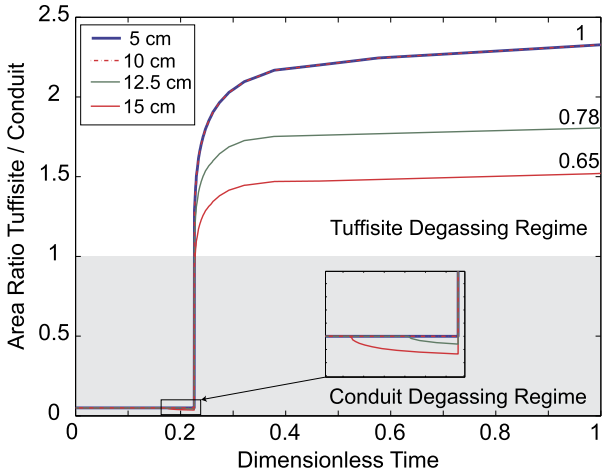

Fig. A5. Summary of the model results showing the evolution of the outgassing capacity (i.e. the ratio of permeable areas) as a function of dimensionless time. The plot shows the results for a 10 m conduit diameter and tuffisites of varying thicknesses. Small numbers indicate the fraction of permeable area retained in the tuffisite upon completion of compaction relative to the initial area.

Tuffisite geometry, on the other hand does affect the area ratio, since the absolute area available for outgassing is affected by the evolution of compaction across the vein. As long as a vein is narrow enough to quench in permeability values above the edifice permeability threshold across its entire cross section, the area available for outgassing remains at the assigned 5% of the conduit area. If, however, the vein is sufficiently wide to allow for compaction to proceed beyond the threshold permeability, the area available for outgassing will reduce. The effect of this process on the overall outgassing budget of a volcano is reported in Fig. A5.

As shown in Appendix A2, both the 5 and 10 cm veins are cooling limited and remain above the edifice permeability threshold (10^{-16} m^2), therefore they plot on along the same line throughout compaction. This means that their entire area remains above the permeability threshold. Their absolute permeability is, however, higher in the more narrow vein due to more efficient quenching (see Figs. A3, A4). Thicker veins (>10 cm), on the other hand, remain sufficiently hot in their interiors so that compaction proceeds further and the central parts of these veins drop below the edifice permeability threshold, resulting in a decreased ratio of tuffisite outgassing area to conduit outgassing area (Fig. A5, y-axis). The small inset in Fig. A5 shows that the tuffisite to conduit outgassing area ratio decreases slightly prior to permeability shut off across the largest part of the conduit. This is because at equal depth, compaction is slightly more efficient in the tuffisite veins as they experience a constant load of the overlying edifice rocks, whereas the load on the conduit deposit is porosity dependent and increases with compaction.

In summary, the model results plotted in Fig. A5 show that (1) tuffisite veins have a higher outgassing capacity than the conduit material for any reasonable tuffisite vein thickness, and (2) under any reasonable geometric circumstances tuffisite outgassing may yield insights to the pressure state of a volcano. The evolution of the gas escape budget (i.e. the partitioning of gas escape between the permeable conduit annulus and tuffisite linked fumaroles) is then largely controlled by the tuffisite vein geometry.

References

Alidibirov, M., Dingwell, D.B., 1996. Magma fragmentation by rapid decompression. Nature 380, 146–148.

Barmin, A., Melnik, O., Sparks, R.S.J., 2002. Periodic behavior in lava dome eruptions. Earth Planet. Sci. Lett. 199 (1), 173–184.

Berlo, K., Tuffen, H., Smith, V., Castro, J., Pyle, D., Mather, T., Geraki, K., 2013. Element variations in rhyolitic magma resulting from gas transport. Geochim. Cosmochim. Acta 121, 436–451.

Bluth, G.J., Rose, W.I., 2004. Observations of eruptive activity at Santiaguito volcano, Guatemala. J. Volcanol. Geotherm. Res. 136 (3–4), 297–302.

Bonaccorso, A., Davis, P.M., 1999. Models of ground deformation from vertical volcanic conduits with application to eruptions of Mount St. Helens and Mount Etna. J. Geophys. Res., Solid Earth 104 (B5), 10531–10542.

Browne, B., Szramek, L., 2015. Chapter 9 – Rates of magma ascent and storage A2. In: Sigurdsson, Haraldur (Ed.), The Encyclopedia of Volcanoes, second edition. Academic Press, Amsterdam, pp. 203–214.

Burgisser, A., Chevalier, L., Gardner, J.E., Castro, J.M., 2017. The percolation threshold and permeability evolution of ascending magmas. Earth Planet. Sci. Lett. 470, 37–47.

Butterfield, D.A., Nakamura, K.-i., Takano, B., Lilley, M.D., Lupton, J.E., Resing, J.A., Roe, K.K., 2011. High SO_2 flux, sulfur accumulation, and gas fractionation at an erupting submarine volcano. Geology 39 (9), 803–806.

Cabrera, A., Weinberg, R.F., Wright, H.M., 2015. Magma fracturing and degassing associated with obsidian formation: the explosive–effusive transition. J. Volcanol. Geotherm. Res. 298, 71–84.

Cabrera, A., Weinberg, R.F., Wright, H.M., Zlotnik, S., Cas, R.A., 2011. Melt fracturing and healing: a mechanism for degassing and origin of silicic obsidian. Geology 39 (1), 67–70.

Campbell, M.E., Russell, J.K., Porritt, L.A., 2013. Thermomechanical milling of accessory lithics in volcanic conduits. Earth Planet. Sci. Lett. 377–378, 276–286.

Carey, S., Sigurdsson, H., 1989. The intensity of plinian eruptions. Bull. Volcanol. 51 (1), 28–40.

Caricchi, L., Burlini, L., Ulmer, P., Gerya, T., Vassalli, M., Papale, P., 2007. Non-Newtonian rheology of crystal-bearing magmas and implications for magma ascent dynamics. Earth Planet. Sci. Lett. 264 (3–4), 402–419.

Carslaw, H., Jaeger, J., 1959. Conduction of Heat in Solids, vol. 302. Oxford University Press, New York, p. 302, 340–341.

Castro, J., Cordonnier, B., Tuffen, H., Tobin, M.J., Puskar, L., Martin, M.C., Bechtel, H.A., 2012. The role of melt-fracture degassing in defusing explosive rhyolite eruptions at volcán Chaitén. Earth Planet. Sci. Lett. 333–334, 63–69.

Castro, J.M., Dingwell, D.B., 2009. Rapid ascent of rhyolitic magma at Chaitén volcano, Chile. Nature 461 (8 Octobre), 780–784.

Chadwick, W.W., Archuleta, R.J., Swanson, D.A., 1988. The mechanics of ground deformation precursory to dome-building extrusions at Mount St. Helens 1981–1982. J. Geophys. Res., Solid Earth. 93 (B5), 4351–4366.

Chevalier, L., Collombet, M., Pinel, V., 2017. Temporal evolution of magma flow and degassing conditions during dome growth, insights from 2D numerical modeling. J. Volcanol. Geotherm. Res. 333, 116–133.

Clarke, A.B., Esposti Ongaro, T., Belousov, A., 2015. Chapter 28 – Vulcanian eruptions A2. In: Sigurdsson, Haraldur (Ed.), The Encyclopedia of Volcanoes, second edition. Academic Press, Amsterdam, pp. 505–518.

Cloos, H., 1941. Bau und Taetigkeit von Tuffschloten; Untersuchungen an dem schwaebischen Vulkan. Trans. Stephan Kolzenburg. Geol. Rundsch. 32, 709–800.

Collinson, A.S.D., Neuberg, J.W., 2012. Gas storage, transport and pressure changes in an evolving permeable volcanic edifice. J. Volcanol. Geotherm. Res. 243, 1–13.

Costa, A., Melnik, O., Sparks, R.S.J., 2007. Controls of conduit geometry and wallrock elasticity on lava dome eruptions. Earth Planet. Sci. Lett. 260 (1), 137–151.

Crank, J., 1979. The Mathematics of Diffusion. Oxford University Press.

De Michieli Vitturi, M., Clarke, A.B., Neri, A., Voight, B., 2008. Effects of conduit geometry on magma ascent dynamics in dome-forming eruptions. Earth Planet. Sci. Lett. 272 (3), 567–578.

Deardorff, N.D., Cashman, K.V., Chadwick, W.W., 2011. Observations of eruptive plume dynamics and pyroclastic deposits from submarine explosive eruptions at NW Rota-1, Mariana arc. J. Volcanol. Geotherm. Res. 202 (1), 47–59.

Delaney, P.T., Pollard, D.D., 1981. Deformation of host rocks and flow of magma during growth of minette dikes and breccia-bearing intrusions near Ship Rock, New Mexico. USGS Prof. Pap. 1202.

Edmonds, M., Oppenheimer, C., Pyle, D.M., Herd, R.A., Thompson, G., 2003. SO_2 emissions from Soufrière Hills Volcano and their relationship to conduit permeability, hydrothermal interaction and degassing regime. J. Volcanol. Geotherm. Res. 124, 23–43.

Eichelberger, J., Carrigan, C., Westrich, H., Price, R., 1986. Non-explosive silicic volcanism. Nature 323, 598–602.

Elders, W.A., Friðleifsson, G.Ó., Albertsson, A., 2014. Drilling into magma and the implications of the Iceland Deep Drilling Project (IDDP) for high-temperature geothermal systems worldwide. Geothermics 49, 111–118.

Embley, R.W., Chadwick, W.W., Baker, E.T., Butterfield, D.A., Resing, J.A., De Ronde, C.E., Tunnicliffe, V., Lupton, J.E., Juniper, S.K., Rubin, K.H., 2006. Long-term eruptive activity at a submarine arc volcano. Nature 441 (7092), 494–497.

Farquharson, J.I., Baud, P., Heap, M.J., 2017a. Inelastic compaction and permeability evolution in volcanic rock. Solid Earth 8 (2), 561.

Farquharson, J.I., Heap, M.J., Lavallée, Y., Varley, N.R., Baud, P., 2016. Evidence for the development of permeability anisotropy in lava domes and volcanic conduits. J. Volcanol. Geotherm. Res. 323, 163–185.

Farquharson, J., Heap, M.J., Varley, N.R., Baud, P., Reuschlé, T., 2015. Permeability and porosity relationships of edifice-forming andesites: a combined field and laboratory study. J. Volcanol. Geotherm. Res. 297, 52–68.

Farquharson, J.I., Wadsworth, F.B., Heap, M.J., Baud, P., 2017b. Time-dependent permeability evolution in compacting volcanic fracture systems and implications for gas overpressure. J. Volcanol. Geotherm. Res. 339, 81–97.

Gardner, J.E., Wadsworth, F.B., Llewellin, E.W., Watkins, J.M., Coumans, J.P., 2018. Experimental sintering of ash at conduit conditions and implications for the longevity of tuffisites. Bull. Volcanol. 80, 23.

Giordano, Russell, J.K., Dingwell, D.B., 2008. Viscosity of magmatic liquids: a model. Earth Planet. Sci. Lett. 271, 123–134.

Gonnermann, H.M., Manga, M., 2003. Explosive volcanism may not be an inevitable consequence of magma fragmentation. Nature (London) 426 (6965), 432–435.

Goto, Y., Nakada, S., Kurokawa, M., Shimano, T., Sugimoto, T., Sakuma, S., Hoshizumi, H., Yoshimoto, M., Uto, K., 2008. Character and origin of lithofacies in the conduit of Unzen volcano, Japan. J. Volcanol. Geotherm. Res. 175 (1), 45–59.

Grunder, A., Russell, J.K., 2005. Welding processes in volcanology: insights from field, experimental, and modeling studies. J. Volcanol. Geotherm. Res. 142, 1–9.

Head, E., Dalton, M., Bluth, G., Rose, W., 2003. Santiaguito Volcano, Guatemala: a study of vent dynamics over the past 50 years. In: Proceedings AGU Fall Meeting Abstracts.

Heap, M.J., Farquharson, J.I., Wadsworth, F.B., Kolzenburg, S., Russell, J.K., 2015. Timescales for permeability reduction and strength recovery in densifying magma. Earth Planet. Sci. Lett. 429, 223–233.

Heap, M.J., Kolzenburg, S., Russell, J.K., Campbell, M.E., Welles, J., Farquharson, J.I., Ryan, A., 2014. Conditions and timescales for welding block-and-ash flow deposits. J. Volcanol. Geotherm. Res.

Heap, M.J., Violay, M., Wadsworth, F.B., Vasseur, J., 2017. From rock to magma and back again: the evolution of temperature and deformation mechanism in conduit margin zones. Earth Planet. Sci. Lett. 463, 92–100.

Heiken, G., Wohletz, K., Eichelberger, J., 1988. Fracture fillings and intrusive pyroclasts, Inyo Domes, California. J. Geophys. Res. 93, 4335–4350.

Hickson, C.J., Russell, J.K., Stasiuk, M.V., 1999. Volcanology of the 2350 B.P. eruption of Mount Meager volcanic complex, British Columbia, Canada; implications for hazards from eruptions in topographically complex terrain. Bull. Volcanol. 60, 489–507.

Holland, A.S.P., Watson, I.M., Phillips, J.C., Caricchi, L., Dalton, M.P., 2011. Degassing processes during lava dome growth: insights from Santiaguito lava dome, Guatemala. J. Volcanol. Geotherm. Res. 202, 153–166.

Jaupart, C., Allègre, C.J., 1991. Gas content, eruption rate and instabilities of eruption regime in silicic volcanoes. Earth Planet. Sci. Lett. 102, 413–429.

Jellinek, A.M., Bercovici, D., 2011. Seismic tremors and magma wagging during explosive volcanism. Nature 470 (7335), 522–525.

Kano, K., Matsuura, H., Yamauchi, S., 1997. Miocene rhyolitic welded tuff infilling a funnel-shaped eruption conduit Shiotani, southeast of Matsue, SW Japan. Bull. Volcanol. 59 (2), 125–135.

Kendrick, J.E., Lavallée, Y., Varley, N.R., Wadsworth, F.B., Lamb, O.D., Vasseur, J., 2016. Blowing off steam: tuffisite formation as a regulator for lava dome eruptions. Front. Earth Sci. 4.

Kennedy, B.M., Jellinek, A.M., Russell, J.K., Nichols, A.R.L., Vigouroux, N., 2010. Time- and temperature-dependent conduit wall porosity: a key control on degassing and explosivity at Tarawera volcano, New Zealand. Earth Planet. Sci. Lett. 299, 126–137.

Klug, C., Cashman, K.V., 1996. Permeability development in vesiculating magmas: implications for fragmentation. Bull. Volcanol. 58, 87–100.

Kolzenburg, S., Heap, M.J., Lavallée, Y., Russell, J.K., Meredith, P.G., Dingwell, D.B., 2012. Strength and permeability recovery of tuffisite-bearing andesite. Solid Earth 3, 191–198.

Kolzenburg, S., Russell, J., 2014. Welding of pyroclastic conduit infill: a mechanism for cyclical explosive eruptions. J. Geophys. Res., Solid Earth 119, 5305–5323.

Kolzenburg, S., Russell, J.K., Kennedy, L.A., 2013. Energetics of glass fragmentation: experiments on synthetic and natural glasses. Geochem. Geophys. Geosyst. 14 (11), 4936–4951.

Lavallée, Y., Varley, N., Alatorre-Ibargüengoitia, M., Hess, K.-U., Kueppers, U., Mueller, S., Richard, D., Scheu, B., Spieler, O., Dingwell, D., 2012. Magmatic architecture of dome-building eruptions at Volcán de Colima, Mexico. Bull. Volcanol. 74, 249–260.

Lesti, C., Porreca, M., Giordano, G., Mattei, M., Cas, R.F., Wright, H.N., Folkes, C., Viramonte, J., 2011. High-temperature emplacement of the Cerro Galán and Toconquis Group ignimbrites (Puna plateau, NW Argentina) determined by TRM analyses. Bull. Volcanol. 73, 1535–1565.

Liu, Y., Zhang, Y., Behrens, H., 2005. Solubility of H_2O in rhyolitic melts at low pressures and a new empirical model for mixed H_2O–CO_2 solubility in rhyolitic melts. J. Volcanol. Geotherm. Res. 143, 219–235.

Macedonio, G., Costa, A., Folch, A., 2008. Ash fallout scenarios at Vesuvius: numerical simulations and implications for hazard assessment. J. Volcanol. Geotherm. Res. 178 (3), 366–377.

Mangan, M., Mastin, L., Sisson, T., 2004. Gas evolution in eruptive conduits: combining insights from high temperature and pressure decompression experiments with steady-state flow modeling. J. Volcanol. Geotherm. Res. 129 (1), 23–26.

Massol, H., Jaupart, C., 1999. The generation of gas overpressure in volcanic eruptions. Earth Planet. Sci. Lett. 166, 57–70.

McGowan, E., Tuffen, H., James, M., Wynn, P., 2016. Magma deformation and emplacement in rhyolitic dykes. In: Proceedings EGU General Assembly Conference Abstracts, vol. 18.

McNutt, S.R., Thompson, G., Johnson, J., Angelis, S.D., Fee, D., 2015. Chapter 63 – Seismic and infrasonic monitoring A2. In: Sigurdsson, Haraldur (Ed.), The Encyclopedia of Volcanoes, second edition. Academic Press, Amsterdam, pp. 1071–1099.

Melnik, O., Sparks, R., 1999. Nonlinear dynamics of lava dome extrusion. Nature 402 (6757), 37–41.

Molina, I., Kumagai, H., Yepes, H., 2004. Resonances of a volcanic conduit triggered by repetitive injections of an ash-laden gas. Geophys. Res. Lett. 31.

Neri, A., Dobran, F., 1994. Influence of eruption parameters on the thermofluid dynamics of collapsing volcanic columns. J. Geophys. Res., Solid Earth 99 (B6), 11833–11857.

Neuberg, J., 2000. Characteristics and causes of shallow seismicity in andesite volcanoes. Philos. Trans. R. Soc. Lond. A, Math. Phys. Eng. Sci. 358 (1770), 1533–1546.

Paisley, R., Berlo, K., Ghaleb, B., Tuffen, H., 2019. Geochemical constraints on the role of tuffisite veins in degassing at the 2008–09 Chaitén and 2011–12 Cordón Caulle rhyolite eruptions. J. Volcanol. Geotherm. Res.

Papale, P., 1999. Numerical simulations of magma ascent along volcanic conduits. Phys. Chem. Earth, Part A, Solid Earth Geod. 24 (11–12), 957–961.

Quane, S.L., Russell, J.K., 2003. Rock strength as a metric of welding intensity in pyroclastic deposits. Eur. J. Mineral. 15, 855–864.

Quane, S.L., Russell, J.K., 2005. Welding insights from high-temperature analogue experiments. J. Volcanol. Geotherm. Res. 142, 67–87.

Quane, S.L., Russell, J.K., Friedlander, E.A., 2009. Time scales of compaction in volcanic systems. Geology 37, 471–474.

Russell, J.K., Quane, S.L., 2005. Rheology of welding; inversion of field constraints. J. Volcanol. Geotherm. Res. 142, 173–191.

Rust, A.C., Cashman, K.V., 2004. Permeability of vesicular silicic magma: inertial and hysteresis effects. Earth Planet. Sci. Lett. 228, 93–107.

Rutherford, M.J., Hill, P.M., 1993. Magma ascent rates from amphibole breakdown: an experimental study applied to the 1980—1986 Mount St. Helens eruptions. J. Geophys. Res., Solid Earth 98 (B11), 19667–19685.

Rutherford, M.J., Sigurdsson, H., Carey, S., Davis, A., 1985. The May 18, 1980, eruption of Mount St. Helens, 1: melt composition and experimental phase equilibria. J. Geophys. Res., Solid Earth 90, 2929–2947.

Ryan, A.G., Friedlander, E.A., Russell, J.K., Heap, M.J., Kennedy, L.A., 2018. Hot pressing in conduit faults during lava dome extrusion: insights from Mount St. Helens 2004–2008. Earth Planet. Sci. Lett. 482, 171–180.

Ryan, A.G., Russell, J.K., Nichols, A.R., Hess, K.-U., Porritt, L.A., 2015. Experiments and models on H_2O retrograde solubility in volcanic systems. Am. Mineral. 100, 774–786.

Rymer, H., Murray, J.B., Brown, G.C., Ferrucci, F., McGuire, W.J., 1993. Mechanisms of magma eruption and emplacement at Mt Etna between 1989 and 1992. Nature 361 (6411), 439–441.

Saubin, E., Tuffen, H., Gurioli, L., Owen, J., Castro, J.M., Berlo, K., McGowan, E.M., Schipper, C.I., Wehbe, K., 2016. Conduit dynamics in transitional rhyolitic activity recorded by tuffisite vein textures from the 2008–2009 Chaitén eruption. Front. Earth Sci. 4, 59.

Schauroth, J., Wadsworth, F.B., Kennedy, B., von Aulock, F.W., Lavallée, Y., Damby, D.E., Vasseur, J., Scheu, B., Dingwell, D.B., 2016. Conduit margin heating and deformation during the AD 1886 basaltic Plinian eruption at Tarawera volcano, New Zealand. Bull. Volcanol. 78, 12.

Schipper, C.I., Castro, J.M., Tuffen, H., James, M.R., How, P., 2013. Shallow vent architecture during hybrid explosive–effusive activity at Cordón Caulle (Chile, 2011–12): evidence from direct observations and pyroclast textures. J. Volcanol. Geotherm. Res. 262, 25–37.

Schneider, A., Rempel, A.W., Cashman, K.V., 2012. Conduit degassing and thermal controls on eruption styles at Mount St. Helens. Earth Planet. Sci. Lett. 357–358, 347–354.

Shea, T., Gurioli, L., Houghton, B.F., Cioni, R., Cashman, K.V., 2011. Column collapse and generation of pyroclastic density currents during the AD 79 eruption of Vesuvius: the role of pyroclast density. Geology 39 (7), 695–698.

Sigurdsson, H., Houghton, B., McNutt, S., Rymer, H., Stix, J., 2015. The Encyclopedia of Volcanoes. Elsevier.

Sparks, R., Murphy, M., Lejune, A., Watts, R., Barclay, J., Young, S., 2000. Control on the emplacement of the andesite lava dome of the Soufriere Hills volcano, Montserrat by degassing-induced crystallisation. Terra Nova 12, 1–20.

Sparks, R.S.J., Tait, S.R., Yanev, Y., 1999. Dense welding caused by volatile resorption. Q. J. Geol. Soc. Lond. 156 (Part 2), 217–225.

Stasiuk, M.V., Barclay, J., Carroll, M.R., Jaupart, C., Ratte, J.C., Sparks, R.S.J., Tait, S.R., 1996. Degassing during magma ascent in the Mule Creek vent (USA). Bull. Volcanol. 58 (2–3), 117–130.

Swanson, D., Holcomb, R., 1990. Regularities in growth of the Mount St. Helens dacite dome, 1980–1986. In: Lava Flows and Domes: Emplacement Mechanisms and Hazard Implications, pp. 3–24.

Taran, Y., Gavilanes, J.C., Cortés, A., 2002. Chemical and isotopic composition of fumarolic gases and the SO_2 flux from Volcan de Colima, Mexico, between the 1994 and 1998 eruptions. J. Volcanol. Geotherm. Res. 117, 105–119.

Taran, Y.A., Bernard, A., Gavilanes, J.C., Lunezheva, E., Cortes, A., Armienta, M.A., 2001. Chemistry and mineralogy of high-temperature gas discharges from Colima volcano, Mexico. Implications for magmatic gas-atmosphere interaction. J. Volcanol. Geotherm. Res. 108, 245–264.

Tuffen, H., Dingwell, D., 2004. Fault textures in volcanic conduits: evidence for seismic trigger mechanisms during silicic eruptions. Bull. Volc. 67 (4), 370–387.

Tuffen, H., Dingwell, D.B., Pinkerton, H., 2003. Repeated fracture and healing of silicic magma generate flow banding and earthquakes? Geology 31, 1089–1092.

Tuffen, H., Smith, R., Sammonds, P.R., 2008. Evidence for seismogenic fracture of silicic magma. Nature 453, 511–514.

Vallance, J.W., Schneider, D.J., Schilling, S.P., 2008. Growth of the 2004—2006 lava-dome complex at Mount St. Helens, Washington. In: A Volcano Rekindled, pp. 2004–2006.

Vasseur, J., Wadsworth, F.B., Lavallée, Y., Hess, K.-U., Dingwell, D.B., 2013. Volcanic sintering: timescales of viscous densification and strength recovery. Geophys. Res. Lett. 40, 5658–5664.

Vespermann, D., Schmincke, H.-U., 2000. Scoria Cones and Tuff Rings. Academic Press.

Vetere, F., Iezzi, G., Behrens, H., Holtz, F., Ventura, G., Misiti, V., Cavallo, A., Mollo, S., Dietrich, M., 2015. Glass forming ability and crystallisation behaviour of sub-alkaline silicate melts. Earth-Sci. Rev. 150, 25–44.

Wadsworth, F.B., Vasseur, J., Aulock, F.W., Hess, K.U., Scheu, B., Lavallée, Y., Dingwell, D.B., 2014. Nonisothermal viscous sintering of volcanic ash. J. Geophys. Res., Solid Earth.

Wadsworth, F.B., Vasseur, J., Scheu, B., Kendrick, J.E., Lavallée, Y., Dingwell, D.B., 2016. Universal scaling of fluid permeability during volcanic welding and sediment diagenesis. Geology 44, 219–222.

Walker, S.L., Baker, E.T., Resing, J.A., Chadwick, W.W., Lebon, G.T., Lupton, J.E., Merle, S.G., 2008. Eruption-fed particle plumes and volcaniclastic deposits at a submarine volcano: NW Rota-1, Mariana Arc. J. Geophys. Res., Solid Earth 113 (B8).

Watts, R., Herd, R., Sparks, R., Young, S., 2002. Growth patterns and emplacement of the andesitic lava dome at Soufriere Hills Volcano, Montserrat. Geol. Soc. Lond. 21 (1), 115–152.

Wilson, L., Sparks, R.S.J., Walker, G.P., 1980. Explosive volcanic eruptions—IV. The control of magma properties and conduit geometry on eruption column behaviour. Geophys. J. Int. 63 (1), 117–148.

Wright, H.M.N., Cashman, K.V., 2014. Compaction and gas loss in welded pyroclastic deposits as revealed by porosity, permeability, and electrical conductivity measurements of the Shevlin Park Tuff. Geol. Soc. Am. Bull. 126, 234–247.